

REPORT DOCUMENTATION PAGE				Form Approved OMB NO. 0704-0188	
<p>The public reporting burden for this collection of information is estimated to average 1 hour per response, including the time for reviewing instructions, searching existing data sources, gathering and maintaining the data needed, and completing and reviewing the collection of information. Send comments regarding this burden estimate or any other aspect of this collection of information, including suggestions for reducing this burden, to Washington Headquarters Services, Directorate for Information Operations and Reports, 1215 Jefferson Davis Highway, Suite 1204, Arlington VA, 22202-4302. Respondents should be aware that notwithstanding any other provision of law, no person shall be subject to any penalty for failing to comply with a collection of information if it does not display a currently valid OMB control number.</p> <p>PLEASE DO NOT RETURN YOUR FORM TO THE ABOVE ADDRESS.</p>					
1. REPORT DATE (DD-MM-YYYY) 12-03-2011		2. REPORT TYPE Final Report		3. DATES COVERED (From - To) 1-May-2008 - 31-Oct-2010	
4. TITLE AND SUBTITLE Final Report: A Computational Investigation of Nanoelectromechanical Switches				5a. CONTRACT NUMBER W911NF-08-1-0061	
				5b. GRANT NUMBER	
				5c. PROGRAM ELEMENT NUMBER 611102	
6. AUTHORS Horacio Espinosa				5d. PROJECT NUMBER	
				5e. TASK NUMBER	
				5f. WORK UNIT NUMBER	
7. PERFORMING ORGANIZATION NAMES AND ADDRESSES Northwestern University Evanston Campus 633 Clark Street Crown Center Room 2-502 Evanston, IL 60208 -1110				8. PERFORMING ORGANIZATION REPORT NUMBER	
9. SPONSORING/MONITORING AGENCY NAME(S) AND ADDRESS(ES) U.S. Army Research Office P.O. Box 12211 Research Triangle Park, NC 27709-2211				10. SPONSOR/MONITOR'S ACRONYM(S) ARO	
				11. SPONSOR/MONITOR'S REPORT NUMBER(S) 53051-EG.1	
12. DISTRIBUTION AVAILABILITY STATEMENT Approved for Public Release; Distribution Unlimited					
13. SUPPLEMENTARY NOTES The views, opinions and/or findings contained in this report are those of the author(s) and should not be construed as an official Department of the Army position, policy or decision, unless so designated by other documentation.					
14. ABSTRACT The International Technology Roadmap for Semiconductors (ITRS) identifies emerging technologies with the potential to sustain Moore's Law. A necessary succession from planar CMOS to non-planar/dual-gate CMOS, and ultimately to novel architectures such as carbon nanotube- (CNT)-based nanoelectromechanical systems (NEMS) is envisioned. The ITRS also identifies critical roadblocks currently precluding advances beyond CMOS. Primary among the roadblocks to NEMS are poor reliability and manufacturing challenges. Here we investigate, both					
15. SUBJECT TERMS					
16. SECURITY CLASSIFICATION OF:			17. LIMITATION OF ABSTRACT UU	15. NUMBER OF PAGES	19a. NAME OF RESPONSIBLE PERSON Horacio Espinosa
a. REPORT UU	b. ABSTRACT UU	c. THIS PAGE UU			19b. TELEPHONE NUMBER 847-467-5989

Report Title

Final Report: A Computational Investigation of Nanoelectromechanical Switches

ABSTRACT

The International Technology Roadmap for Semiconductors (ITRS) identifies emerging technologies with the potential to sustain Moore's Law. A necessary succession from planar CMOS to non-planar/dual-gate CMOS, and ultimately to novel architectures such as carbon nanotube- (CNT)-based nanoelectromechanical systems (NEMS) is envisioned. The ITRS also identifies critical roadblocks currently precluding advances beyond CMOS. Primary among the roadblocks to NEMS are poor reliability and manufacturing challenges. Here we investigate, both computationally and experimentally, the prevalent failure modes of CNT-based NEMS that hamper reliability. We first identify their point of onset within the design space, highlighting the extremely limited region in which failure is currently avoided. We use dynamic multiphysics models to elucidate the underlying causes of failure, and then show that the usable design space expands dramatically when employing novel electrode materials such as diamond-like carbon. We then demonstrate the efficacy of this solution through numerous successive actuation cycles without failure and applications to volatile memory operations. Finally, we develop a probe-based nanomanufacturing scheme by which to scale up manufacturing of these robust devices. Ultimately, these advances will be critical in delivering a broad class of robust, battle-ready NEMS sensors and electronics.

List of papers submitted or published that acknowledge ARO support during this reporting period. List the papers, including journal references, in the following categories:

(a) Papers published in peer-reviewed journals (N/A for none)

O. Loh, X. Wei, C. Ke, J. Sullivan, and H.D. Espinosa "Robust Carbon-Nanotube-Based Nano-electromechanical Devices: Understanding and Eliminating Prevalent Failure Modes Using Alternative Electrode Materials" Small, Volume 7, No 1, p 79-86, 2011.

R. Agrawal, O. Loh and H. D. Espinosa "The Evolving Role of Experimental Mechanics in 1-D Nanostructure-Based Device Development" Experimental Mechanics, Volume 51, Number 1, 1-9, DOI: 10.1007/s11340-010-9437-0

Number of Papers published in peer-reviewed journals: 2.00

(b) Papers published in non-peer-reviewed journals or in conference proceedings (N/A for none)

Number of Papers published in non peer-reviewed journals: 0.00

(c) Presentations

H. Espinosa, O. Loh, X. Wei. Robust Carbon Nanotube-Based NEMS: Understanding and Eliminating Prevalent Failure Modes Using Alternative Electrode Materials. Materials Research Society Fall Meeting, Boston, MA. November, 2010.

O. Loh, X. Wei, K. Nandy, and H. Espinosa. Arrays of robust carbon nanotube-based NEMS: A combined experimental/computational investigation. Society for Experimental Mechanics Annual Conf. On Experimental and Applied Mechanics. Indianapolis, IN. June, 2010.

O. Loh and H. D. Espinosa. Nanofountain probes for direct-write nanomanufacturing and in vitro single cell studies. IEEE Int'l. NanoElectronics Conference, Hong Kong, China. January, 2010.

Number of Presentations: 3.00

Non Peer-Reviewed Conference Proceeding publications (other than abstracts):

Number of Non Peer-Reviewed Conference Proceeding publications (other than abstracts): 0

Peer-Reviewed Conference Proceeding publications (other than abstracts):

(d) Manuscripts

O. Loh, X. Wei, J. Sullivan, L. Ocola, R. Divan, H. Espinosa, "Robust carbon-carbon nanoelectromechanical switches," submitted.

Number of Manuscripts:1.00

Patents Submitted

H. Espinosa, O. Loh, and X. Wei, "Electrodes to Improve Reliability of Nanoelectromechanical Systems," serial number 61/397,981

Patents Awarded

Awards

Graduate Students

<u>NAME</u>	<u>PERCENT SUPPORTED</u>
Krishanu Nandy	0.25
Ravi Agrawal	0.05
FTE Equivalent:	0.30
Total Number:	2

Names of Post Doctorates

<u>NAME</u>	<u>PERCENT SUPPORTED</u>
Mohammad Naraghi	0.25
FTE Equivalent:	0.25
Total Number:	1

Names of Faculty Supported

<u>NAME</u>	<u>PERCENT SUPPORTED</u>	National Academy Member
Horacio Espinosa	0.08	No
FTE Equivalent:	0.08	
Total Number:	1	

Names of Under Graduate students supported

<u>NAME</u>	<u>PERCENT SUPPORTED</u>
FTE Equivalent:	
Total Number:	

Student Metrics

This section only applies to graduating undergraduates supported by this agreement in this reporting period

The number of undergraduates funded by this agreement who graduated during this period: 0.00

The number of undergraduates funded by this agreement who graduated during this period with a degree in science, mathematics, engineering, or technology fields:..... 0.00

The number of undergraduates funded by your agreement who graduated during this period and will continue to pursue a graduate or Ph.D. degree in science, mathematics, engineering, or technology fields:..... 0.00

Number of graduating undergraduates who achieved a 3.5 GPA to 4.0 (4.0 max scale): 0.00

Number of graduating undergraduates funded by a DoD funded Center of Excellence grant for Education, Research and Engineering:..... 0.00

The number of undergraduates funded by your agreement who graduated during this period and intend to work for the Department of Defense 0.00

The number of undergraduates funded by your agreement who graduated during this period and will receive scholarships or fellowships for further studies in science, mathematics, engineering or technology fields: 0.00

Names of Personnel receiving masters degrees

NAME

Total Number:

Names of personnel receiving PhDs

NAME

Ravi Agrawal

Total Number:

1

Names of other research staff

NAME

PERCENT SUPPORTED

FTE Equivalent:

Total Number:

Sub Contractors (DD882)

Inventions (DD882)

Scientific Progress

see attachment

Technology Transfer

FINAL REPORT (W911NF0810061): A Combined Experimental/Computational Investigation of Nanoelectromechanical Switches – Understanding and Eliminating Prevalent Failure Modes

ABSTRACT

The International Technology Roadmap for Semiconductors (ITRS¹) identifies emerging technologies with the potential to sustain Moore's Law. A necessary succession from planar CMOS to non-planar/dual-gate CMOS, and ultimately to novel architectures such as carbon nanotube- (CNT)-based nanoelectromechanical systems (NEMS) is envisioned. The ITRS also identifies critical roadblocks currently precluding advances beyond CMOS. Primary among the roadblocks to NEMS are poor reliability and manufacturing challenges. Here we investigate, both computationally and experimentally, the prevalent failure modes of CNT-based NEMS that hamper reliability. We first identify their point of onset within the design space, highlighting the extremely limited region in which failure is currently avoided. We use dynamic multiphysics models to elucidate the underlying causes of failure, and then show that the usable design space expands dramatically when employing novel electrode materials such as diamond-like carbon. We then demonstrate the efficacy of this solution through numerous successive actuation cycles without failure and applications to volatile memory operations. Finally, we develop a probe-based nanomanufacturing scheme by which to scale up manufacturing of these robust devices. Ultimately, these advances will be critical in delivering a broad class of robust, battle-ready NEMS sensors and electronics.

1. OBJECTIVES

NEMS technologies are widely pursued for various applications where technological demands require reduced component size and cost, while dramatically increasing device performance and functionality. These competing factors present significant challenges in device design. Within this project, we develop a platform CNT-NEMS architecture, focusing on understanding the failure modes that are prevalent to this class of devices and

ultimately on overcoming them to allow robust application to memory systems and sensors. Upon successfully overcoming the prevalent failure modes, we turn to develop manufacturing schemes that will allow construction of large-scale arrays of these robust devices. Specifically, our objectives are to:

1. Investigate emerging CNT-NEMS technologies, which are likely to become the next generation of electronic devices and sensors.
2. Perform a dynamic analysis of the device and investigate its performance in the context of applications such as NEMS switches, sensors, random-access memory elements, and logic devices.
3. Experimentally identify prevalent device failure modes and their point of onset within the design space.
4. Employ multiphysics modeling to study the devices' dynamic pull-in response and explain the underlying mechanisms for experimentally-observed failure modes.
5. Computationally predict conditions (device geometry and pull-in voltage) under which device failure is likely and design new architectures devoid of these failure modes.
6. Develop manufacturing schemes to fabricate large-scale arrays of these robust devices.
7. Train graduate students and post-docs in a multidisciplinary environment.

Ultimately, accomplishing these objectives will demonstrate the feasibility of transitioning CNT-NEMS from the lab bench to the battle field in the form of *truly robust, highly functional* devices.

2. INTRODUCTION & SIGNIFICANCE

The immense potential of CNT-based NEMS is emergent in theoretical and experimental demonstrations of up to 100-GHz switching², low leakage and high ON-OFF ratios³, and outstanding current-carrying capacity⁴⁻⁵. To date however, individual demonstrations of performance such as these have been a primary focus, with limited reports of repeated actuation beyond a few cycles^{2-3,6-7}. This is due in large part to critical challenges in device reliability and manufacturing. As a consequence of their ultra-high performance, these devices experience extreme (and coupled) mechanical, electrical, and thermal loads during normal operation. Furthermore, previously insignificant forces (e.g., van der Waals interactions) begin to dominate at this scale. These factors

combine to create a number of failure modes that are prevalent among reported devices. Thus finding a solution to suppress or eliminate the onset of failure is critical to the widespread integration of CNT-based NEMS and will represent a significant milestone along the ITRS path.

Given solutions to these failure modes, scaling up manufacturing to produce large-scale arrays of CNT-NEMS poses another significant ITRS roadblock. The serial methods used to produce the aforementioned devices are in general not conducive to scaling up. For example, electron beam lithography is perhaps the most commonly used method to define electrical contacts to randomly dispersed carbon nanotubes. However, this inherently serial process requires involved imaging, alignment, and pattern generation steps tailored specifically to each individual nanostructure. To date, no method exists to create large-scale arrays of well-ordered individual carbon nanotubes that is readily integrated with other microfabrication processes to construct functional devices.

In this work, an electrostatically-actuated CNT switch⁸⁻¹³ serves as a platform to study prevalent failure modes in CNT-based NEMS and methods by which to scale up manufacturing. This switch is chosen because it shares operating principles (and thus failure modes and manufacturing challenges) with many reported devices, making the findings of this study broadly applicable¹⁴⁻¹⁵. The device consists of a multi-walled CNT of length L that is fixed at one end and cantilevered a distance H above an electrode (Figure 1a). The electrical circuit is completed by a voltage source, V , and an external resistor, R_f . When the applied bias exceeds a critical “pull-in voltage” ($V > V_{PI}$), the CNT accelerates toward the electrode, closing the switch. Subsequent reduction of the applied bias results in re-opening of the switch⁸. The electrical domain can be represented by an equivalent lumped-element circuit (Figure 1b) comprised of the voltage source and external resistor in series with, in parallel, the parasitic capacitance of the system C_0 , the capacitance of the CNT cantilever relative to the electrode C_{CNT} , and the tunneling/contact resistance, R_{CNT} , when the CNT approaches and makes contact with the electrode. Note that C_{CNT} and R_{CNT} will depend upon H (see Section 4.1). The total current is denoted as I_{total} , while the current through the CNT is I_{CNT} . U is the potential across the CNT, where $U = V$ when $I_{total} = 0$.

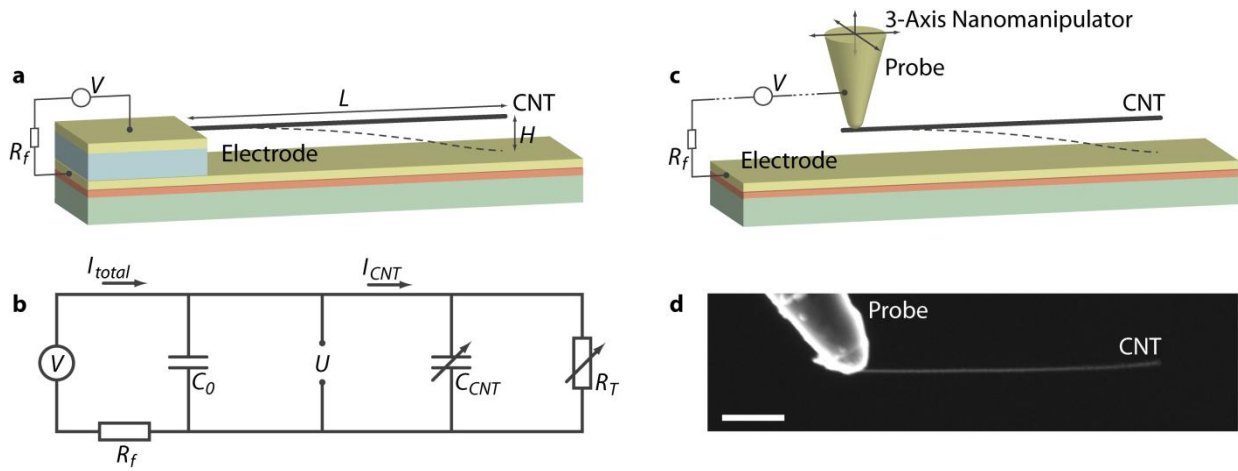


Figure 1 Overview of cantilevered CNT switch used as a platform to study failure modes. (a) Schematic of switch consisting of a CNT cantilevered over a metal thin film electrode. (b) Equivalent lumped-element circuit for the device. (c) Nanomanipulation-based experimental setup used to recreate the device geometry shown in (a), enabling real-time incremental variation of device geometry and simultaneous electromechanical characterization *in situ* the SEM. The voltage source V is the only component exterior to the SEM chamber. (d) Scanning electron micrograph showing a CNT mounted on the tip of a nanomanipulator probe approaching the electrode. Scale bar is 1 μm .

3. EXPERIMENTAL IDENTIFICATION OF FAILURE MODES

A parametric study was first conducted to identify prevalent failure modes and their point of onset within the device design space. To test a large number of device geometries spanning the design space in a more statistically-significant study, an *in situ* nanomanipulation-based technique was adopted over conventional microfabrication processes to construct the devices. A 3-axis nanomanipulator was used to position cantilevered CNTs over an electrode (Figure 1c-d, see Section 7.1), effectively recreating the platform device (Figure 1a). This allowed real-time prescription of device geometry with simultaneous voltage application (V), measurement of total current (I_{total}), and imaging of device operation and failure via SEM. For example, a device of a given length (L) could be repeatedly characterized with incrementally decreasing gap (H) by using the manipulator to progressively step the CNT closer to the electrode. In this initial parametric study, a gold-coated substrate was used as an electrode as reported devices ubiquitously use metal thin film electrodes^{3,8,16-18}.

Two common modes of failure were observed in the initial experiments (Figure 2). For relatively long cantilevers and small CNT-electrode gaps, irreversible stiction preventing re-opening of the switch was observed (Figure 2a-c,f). The corresponding measured I_{total} -V response (Figure 2a) shows a well-defined jump in current upon pull-in, followed by a linear decrease to zero as the applied voltage is ramped back down. This linear behavior is characteristic of maintained Ohmic contact between the CNT and electrode. Imaging the device following actuation confirmed that the CNT indeed remained stuck to the electrode after the applied bias was fully released (Figure 2c). This irreversible stiction has been widely reported and is known to be the result of strong van der Waals interactions between the CNT and electrode^{2,6,16,19-20}. When these adhesive interactions exceed the elastic restoring force in the deformed cantilever, the switch does not re-open, even when the bias is fully removed. In fact, nanotube-substrate interactions have been shown in some cases to be sufficiently strong to radially collapse the CNT²¹⁻²². In cases where the device is operated in atmosphere, liquid adhesion adds additional adhesive energy to be overcome.

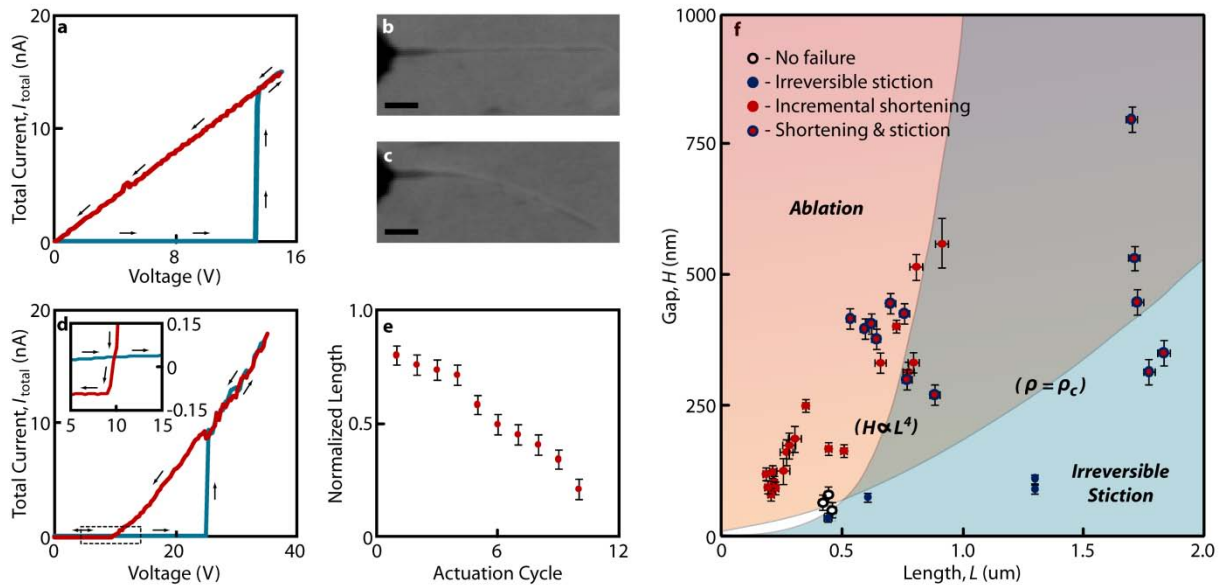


Figure 2 Characteristic failure modes. (a-c) Failure by irreversible CNT-electrode stiction. (a) Characteristic measured I_{total} -V response for a device exhibiting irreversible stiction upon pull-in. Voltage was applied in a single 0-15 V triangle wave. (b,c) Scanning electron micrographs showing the CNT cantilever before and after the actuation cycle respectively. In (c), the CNT clearly remains stuck to the electrode after removing the applied bias. Scale bars are 250 nm. (d-e) Failure by incremental loss of CNT length. (d) Characteristic

measured I_{total} - V response for a device that does not suffer from irreversible stiction. Voltage was applied in a single 0-35 V triangle wave. As the voltage is ramped down after pull-in, the current falls slightly non-linearly until pull-out. Inset shows detail of the pull-out event, after which the current is slightly negative due to gradual discharging of the capacitances, C_0 and C_{CNT} , as the applied voltage continues to decrease. (e) Plot of CNT length (normalized by length before first actuation cycle) following 10 successive actuation cycles. (e) Length of CNT cantilever after successive actuation cycles exhibiting incremental loss. Length is normalized by the initial length before the first cycle. (f) Map of device geometries tested in the L - H design space and the corresponding failure modes observed. Lines indicate analytically-derived boundaries between failure modes (see Section 4.4). Below a critical elastic restoring force, irreversible stiction is expected as adhesive forces dominate. Above a critical current density ($\rho = \rho_c$), CNT ablation is expected upon pull in due to Joule heating.

For relatively short cantilevers with larger CNT-electrode gaps, incremental shortening of the CNT cantilever was observed with successive actuation cycles (Figure 2d-f). Here the characteristic I_{total} - V curve exhibits a sharp drop in current (inset of Figure 2d) as the voltage is ramped down after pull in, signifying successful re-opening of the switch. However, inspection of the CNT after successive actuation cycles revealed an incremental loss of length (Figure 2e). Similar incremental losses have been reported, as well as more extreme cases of complete loss of the CNT^{8,23-25}. Two possible causes are envisioned. During the highly-dynamic pull-in event, the CNT experiences large mechanical stresses as it impacts the electrode at high velocity, which could fracture the CNT. Alternatively, Joule heating resulting from large currents could ablate the nanostructure, resulting in similar loss of length²³⁻²⁶.

4. DYNAMIC MULTIPHYSICS SIMULATIONS TO EXPLAIN FAILURE

To investigate the underlying cause for the observed incremental loss and test potential solutions, a dynamic multiphysics finite element model of the device was developed using ABAQUS/Explicit and appropriate user-defined subroutines. This model, which includes consideration for electrostatic forces and van der Waals interactions between the CNT and substrate, enabled detailed analysis of the time history of the mechanical stresses and electrical current in the CNT.

4.1 Development of Model

In the model, the sum of the attractive van der Waals force and electrostatic force on the CNT were treated as a body force and implemented through the VLOAD subroutine. The repulsive van der Waals force was used to simulate the interaction between the CNT and the substrate and implemented through the VUINTER subroutine.

The dynamic response of the CNT is described as²⁷⁻²⁸

$$\rho A \frac{\partial^2 r}{\partial t^2} + c \frac{\partial r}{\partial t} + EI \frac{\partial^2 r}{\partial x^4} = q_{elec} + q_{vdW}, \quad (1)$$

where $\rho = 2.27 \text{ g/cm}^3$ is the density of the CNT, A is the cross-section area of the CNT, c is the damping constant of the system, E is the elastic modulus and I is the moment of inertia. On the right-hand-side of (1), q_{elec} and q_{vdW} represent the load per unit length on the CNT due to electrostatic and van der Waals interactions, respectively. The damping constant of the system is given as

$$c = \frac{\pi A \rho \omega_0}{Q}, \quad (2)$$

where Q is the quality factor and ω_0 is the natural frequency of the CNT, which can be described as²⁹

$$\omega_0 = \frac{\beta^2}{L^2} \sqrt{\frac{EI}{A\rho}}, \quad (3)$$

where $\beta = 1.875$. The quality factor is taken as 250, which is estimated from the vibration of a CNT cantilever driven by alternating electrical field²⁹.

The electrostatic interaction between a CNT and an electrode has been studied in previous work^{12,30}. The electrostatic force applied per unit length of the CNT is given as

$$q_{elec} = \frac{-\pi \epsilon_0 U^2}{\sqrt{r(r+2R) \cdot a \cosh^2\left(1 + \frac{r}{R}\right)}} (1 + f_c), \quad (4)$$

where ϵ_0 is the permittivity, V is the applied potential on the CNT, r is the gap between the CNT and the substrate, R is the external radius of the CNT, and f_c is a function which considers the concentrated charge effect on the free end of the CNT cantilever¹¹

$$f_c = 0.85[(H + R)^2 R]^{1/3} \delta(x - x_{tip}) \quad (5)$$

in which H is the initial gap between the CNT and substrate.

The van der Waals interaction between the CNT and substrate is calculated based on the Lennard-Jones potential³¹. For the interaction between two atoms with distance, r , the Lennard-Jones potential is

$$\Phi(r) = \frac{C_{12}}{r^{12}} - \frac{C_6}{r^6} \quad (6)$$

in which C_{12} and C_6 are material properties. For carbon-carbon interaction³², $C_{12} = 24.1 \text{ keV } \text{\AA}^{12}$ and $C_6 = 15.2 \text{ keV } \text{\AA}^6$. The potential between an atom and a semi-infinite solid body (with atom density, ρ_1) can be obtained from the integration

$$\Phi(D) = \int_{-\infty}^{+\infty} \int_{-\infty}^{+\infty} \int_{-\infty}^0 \left[\frac{C_{12}}{r^{12}} - \frac{C_6}{r^6} \right] \rho_1 dx dy dz \quad (7)$$

where D is distance between the atom and the semi-infinite solid. Derivative of the potential with respect to D yields the force acting on the atom as

$$f(D) = \frac{\partial \Phi}{\partial D} = \frac{\rho_1 \pi}{5} \left\{ \frac{5C_6}{2D^4} - \frac{C_{12}}{D^{10}} \right\}. \quad (8)$$

Thus, the force acting on a unit volume of atoms (with atom density, ρ_2) is

$$q_{vdW}(D) = \frac{\rho_1 \rho_2 \pi}{5} \left\{ \frac{5C_6}{2D^4} - \frac{C_{12}}{D^{10}} \right\}. \quad (9)$$

In the model, ρ_1 and ρ_2 are set as the atomic density of graphene, $114/\text{nm}^3$.

Therefore, the total attractive force between the CNT and the bottom electrode is the sum of the attractive van der Waals interaction (the first term on the right-hand-side of (9)) and the electrostatic force, and can be written as

$$q_+(D) = \frac{\rho_1 \rho_2 \pi}{5} \frac{5C_6}{2D^4} + \frac{-\pi \epsilon_0 V^2}{2Rt \sqrt{r(r+2R) \cdot a \cosh^2 \left(1 + \frac{r}{R} \right)}} (1 + f_c) \quad (10)$$

The repulsive van der Waals interaction (the second term on the right-hand-side of (9)) is used to define the contact between the CNT and the bottom electrode. Therefore, the normal contact pressure on the CNT is given as

$$q_-(D) = -\frac{\rho_1 \rho_2^S \pi}{5} \frac{C_{12}}{D^{10}} \quad (11)$$

where ρ_2^S represents the number of atoms per unit area. For graphene, $\rho_2^S = 38/\text{nm}^2$.

Since the bias charge on the CNT is time dependent, it is necessary to investigate the equivalent lumped circuit as shown in Figure 1b to obtain the charge on the CNT in real time. The equivalent circuit yields

$$R_f(C_o + C_{CNT}) \frac{dU}{dt} + \left(R_f \frac{dC_{CNT}}{dt} + \frac{R_f}{R_{CNT}} + 1 \right) U = V \quad (12)$$

in which R_f is the feedback resistance, C_o is the capacitance between the two electrodes, R_{CNT} is the tunneling resistance of the CNT to the electrode. In vacuum, the tunneling resistance between the CNT and bottom electrode can be described as $R_{CNT} = R_c \exp(\lambda \delta)$, where R_c is the contact resistance, λ is a constant 22.8 nm^{-1} and δ is the gap between the CNT tip and the substrate³³. In the subroutine, the bias on the CNT, U , is updated at each time step by solving (12) numerically.

4.2 Description of Simulations

To investigate the cause of the observed incremental shortening of the CNT with repeated actuation and test possible solutions, the model described above was setup as follows. In all reported simulations, the CNT cantilever had a length of $1.5 \text{ }\mu\text{m}$, an outer radius of 25 nm , and a wall thickness of 25 shells. The assumption of 25 shells is based on the reported average number of shells for multi-walled CNTs obtained from the same source³⁴. The CNT was modeled as an orthotropic linear elastic material³⁵. Four-node shell elements were used with an element size of 2 nm to investigate the buckling of the CNT during pull-in. The gap between the centerline of the CNT and the electrode was 100 nm . A voltage was applied in a step function of 15 V beginning at $t = 0 \text{ sec}$ to actuate the device.

For cases with a gold electrode, the electrode was modeled as an elastic/plastic material with a Young's modulus of 78 GPa and a Poisson's ratio of 0.44 . A low yield stress of 10 MPa was chosen to count for the softening of Au due to Joule heating. For cases with a diamond-like carbon electrode (tetrahedral amorphous carbon (ta-C), see Section 5), the electrode was modeled as a purely elastic material with a Young's modulus of 87 GPa and a Poisson's ratio of 0.22 . For both cases, a value of $R_f = 1 \text{ G}\Omega$ was used which, in the case of the gold electrode, is representative of the external resistor placed in the circuit (experimentally-measured to be $992 \text{ M}\Omega$). In the case of ta-C, the geometry of the ta-C electrode itself was designed to have a resistance of $1 \text{ G}\Omega$ between the point of CNT contact and its connection to the voltage source (see Section 7.2). Thus no physical

resistor was needed in the circuit, with the resistance of the ta-C electrode/trace taking its place instead. An experimentally-measured value of $C_0 = 50$ pF was used for the parasitic capacitance (see Methods). Experimentally-measured values of contact resistance were used for both cases as well, with $R_c = 50$ k Ω for gold and $R_c = 0.6$ G Ω for ta-C (see Section 7.3). To isolate the effect of the electrode on the device behavior, all other parameters were held constant. Eight-node linear brick elements with reduced integration were used for modeling the bottom electrode.

4.3 Results of Simulations

In the simulations, a step input is given at the voltage source, causing the CNT to pull in. As the CNT strikes the electrode (Figure 3a), a stress wave propagates from the point of contact toward the constrained end, and reflects back (Figure 3c-f). Additionally, minor buckling is observed momentarily along the CNT (Figure 3e). Though significant, the peak stress observed is approximately one order of magnitude less than the reported failure stress for CNTs obtained from the same source²⁷. Thus mechanical fracture alone is an unlikely cause of the observed incremental shortening with repeated actuation (Figure 2e).

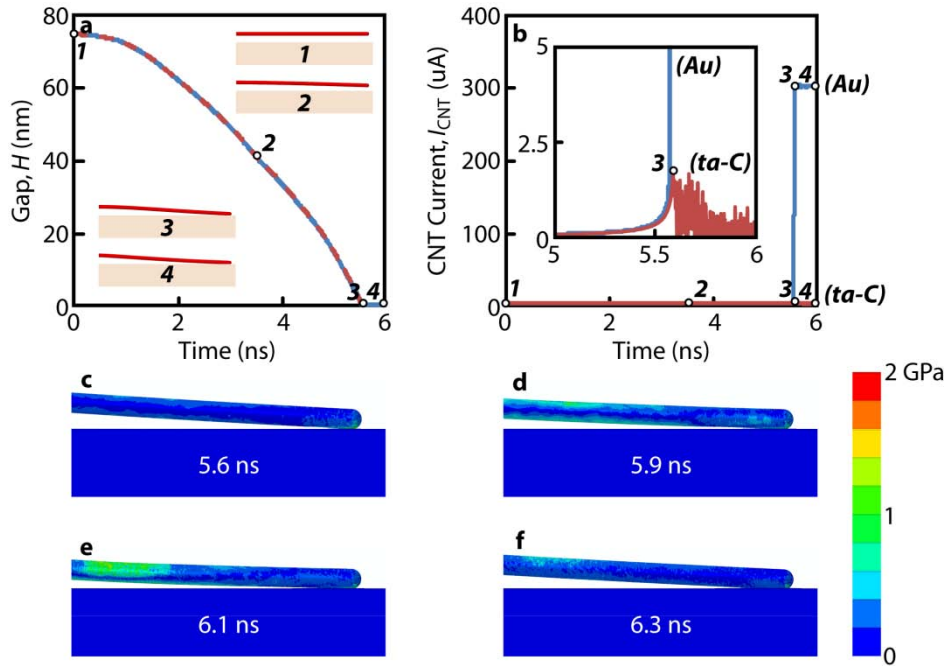


Figure 3 Results of dynamic multiphysics finite element simulation investigating the cause of incremental CNT loss. (a) CNT tip-electrode gap (H) versus time in response to a step in voltage applied at $t = 0$. The response is shown for devices with gold (solid blue line) and ta-C (dashed red line) electrodes. Insets show snapshots of deformed CNT profile as it deflects toward the electrode. (b)

Current through CNT (I_{CNT} , see Figure 1b) versus time for devices with gold and ta-C electrodes. Numbered points along the curves correspond in time to those in (a). (c-f) Snapshots of stress in tip of the CNT during CNT-electrode impact.

Instead of catastrophic mechanical stresses, the dynamic multiphysics analysis reveals a transient spike in current through the CNT (Figure 3b) as it accelerates toward the electrode. This spike, which approaches the mA range, is the result of rapid charge dissipation from the capacitances, C_0 and C_{CNT} (Figure 1b), to the substrate. The corresponding current density (see Section 4.4.1) is more than sufficient to ablate the CNT⁴. In fact, similar observations of incremental loss have been reported in CNT field emitters operated at similar current densities²³⁻²⁵. Plotting a line of constant current density in the L - H design space equivalent to the critical current density required to burn a multi-walled CNT with 25 shells (Figure 2f, see Section 4.4.1) separates well the experimentally-tested cases in which incremental loss was and was not observed, reaffirming the predictions of the model.

During the initial discharge, $I_{CNT} \gg I_{total}$ (Figure 3b). Once the stored charges have been fully depleted and the switch is fully closed, the system reaches a significantly lower steady-state current flow ($I_{total} = I_{CNT} = V/(R_{CNT}+R_f)$, see Figure 1b). Due to the computational cost of the dynamic model, it was not possible to simulate a sufficiently long time period to reach this steady state. However, this steady state current has been previously predicted analytically for similar devices⁸ and is measured in the present experiments (I_{total} , Figure 2a and Figure 5a). Here it is important to note that, based upon the equivalent lumped-element circuit (Figure 1b), the spike in I_{CNT} is not expected to appear in the measured I_{total} - V response (Figure 2d). Because the spike arises due to discharge of the capacitances, it remains within the $R_{CNT}C_0$ loop and does not contribute directly to the measured I_{total} .

4.4 Predicting the Onset of Failure

To test the suspected modes of failure as predicted by the FEM model against the experimental results and thus validate its predictive power, analytically-derived boundaries between the onset of the various failure modes were plotted over the experimentally-observed cases (see Figure 2f and Figure 5e). These boundaries

were derived based upon the assumed modes of failure predicted by the model. Thus their match with the experimental results will support the validity of the model.

4.4.1 Incremental loss of CNT length due to Joule heating-induced ablation

The results of the multiphysics FEM modeling suggest that a significant discharge current occurring when the CNT touches the gold electrode is sufficient to ablate the CNT. This is the result of low CNT-electrode contact resistance leading to a fast time constant for dissipation of charge stored in the system. The reported threshold current density (ρ_c , also known as breakdown current density) is on the order of 10^8 A/cm² for CNTs and graphene^{5,36}. Similar observations of incremental loss from CNTs used as field emitters have been reported for high current densities²³.

When the CNT contacts the bottom electrode, the total charge stored in the system will dissipate rapidly due to the low contact resistance. Given that $U \sim V_{PI}$ at the time of contact, the maximum current density on the CNT can be approximated by

$$\rho_i = \frac{V_{PI}}{R_{CNT}} \frac{1}{2\pi R_{ext} h N}, \quad (14)$$

where R_{ext} is the external radius of the CNT, h is taken as 0.34 nm (the interlayer spacing between CNT shells), and N is the number of shells in the multi-walled CNT. The pull-in voltage is expressed as¹²

$$V_{PI} = 0.85 \sqrt{\frac{1 + \frac{8H^2}{9L^2}}{1 + \frac{2.55[R_{ext}(H+R_{ext})^2]^{1/3}}{L}}} \frac{H}{L^2} \ln\left(\frac{2H}{R_{ext}}\right) \sqrt{\frac{EI}{\epsilon_0}}, \quad (15)$$

where L is the tube length. Combining (14) and (15) and setting $\rho_i = \rho_c$ yields the condition when the outer shell tends to burn when the CNT contacts the Au electrode.

4.4.2 Irreversible stiction due to van der Waals interactions

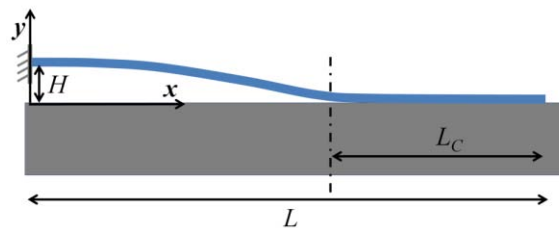


Figure 4 Schematic of stiction of CNT on bottom electrode due to van der Waals interaction.

As the length of the CNT cantilever increases, the CNT tends to stick irreversibly to the bottom electrode after contact. This is because the restoring spring force in the deformed CNT (which decreases with length) cannot overcome the van der Waals interaction with the substrate. Here the stiction length (the length of the CNT that is in contact with the substrate, see Figure 4) is denoted as L_C . When in contact with the substrate, the CNT can thus be treated as a cantilever with a length of $(L - L_C)$ whose left end ($x = 0$) is clamped and at the right end ($x = L - L_C$), the deflection is H with no rotation. The restoring spring force of the cantilever is expressed as

$$F_{re} = \frac{12EIH}{(L-L_C)^3}, \quad (16)$$

The van der Waals interaction can be expressed as

$$F_{vdW} = \alpha L_C, \quad (17)$$

where α is the van der Waals force per unit stiction length. Irreversible stiction occurs when $F_{vdW} \geq F_{re}$, yield a stiction condition of

$$L_C(L - L_C)^3 \geq \frac{12EIH}{\alpha}, \quad (18)$$

with the constraint that $0 < L_C < L$. The right-hand-side of (18) has maximum of $3^3 L^4 / 4^4$ at $L_C = L/4$.

Therefore, the van der Waals stiction yields a profile of constant critical restoring force in the L - H design space (Figures 2f and 4c in the manuscript) which follows $H \propto L^4$. The coefficient in this quartic relation will depend upon the CNT-electrode material interaction, α .

4.5 Using the Model to Redesign the Device Architecture

Looking at the highly limited remaining region of the design space in which no failure is predicted (white region in Figure 2f), it is not surprising to find such limited reports of robust, repeated cycling of electrostatically-actuated CNT-based NEMS. Perhaps the simplest way to avoid ablation would be to reduce the CNT-electrode gap to decrease the required pull-in voltage (and thus the stored charge). However, this promotes stiction. To avoid this, other devices have employed more complex three-terminal electrode configurations in which a gate electrode at high bias is used to push or pull the CNT into contact with a drain electrode at relatively low bias¹⁶⁻

^{17,37-39}. In this way the CNT makes contact only with the drain electrode that is at a relatively small potential difference. However, this requires more complex accessing/multiplexing schemes to scale up and reduces the potential integration density. As such, reports of devices operating without failure or degradation through numerous cycles remain elusive with these architectures.

Examining the equivalent circuit more closely (Figure 1b), increasing R_{CNT} would moderate the detrimental current spike by increasing the time constant for the charge dissipation. However, the contact resistance between CNTs and gold or other conventional metallic electrodes is generally low (measured to be in the k Ω range in our experiments), resulting in rapid discharge and a large current spike at contact²⁶. Unfortunately, simply increasing the external resistor R_f would not have a similar effect as it is outside the $R_{CNT}C_0$ loop and thus does not affect the time constant of the discharge.

Diamond-like carbon (tetrahedral amorphous carbon, ta-C) was next considered as an alternative electrode material. Here the contact resistance between the CNT and electrode was measured to be 0.6 G Ω (see Section 7.3), 5 orders of magnitude greater than for gold. Based upon the previous analysis, this should slow the charge dissipation upon pull-in, thus mitigating the current spike. Before implementing experimentally, this hypothesis was tested using the dynamic multiphysics finite element model. A device of the same geometry was re-simulated with an increased value of contact resistance ($R_{CNT} = 0.6$ G Ω , see Section 7.3). The resulting mechanics of the switch closing are nearly identical, resulting in similar stresses. Figure 3a shows the CNT tip-electrode gap as a function of time in which the cases using gold and ta-C electrodes follow nearly identical paths. By contrast, the spike in current through the CNT drops dramatically as expected in the case of the ta-C electrode. Figure 3b compares the current profile through the CNT using the gold and ta-C electrodes. Here we see that the magnitude of the current spike is less than 2.5 μ A (as compared to > 300 μ A for gold), dropping the resulting current density well below the critical value for burning. As the CNT accelerates toward the electrode (point #3 in Figure 3a-b), a small spike in I_{CNT} is still observed due to the rapidly increasing capacitance with decreasing gap before contact which results in charges being pumped into the CNT. However, because of the increased time

constant for capacitance discharge, the stored charge is dissipated over a significantly longer time, resulting in a peak I_{CNT} current closer to the steady-state measured current.

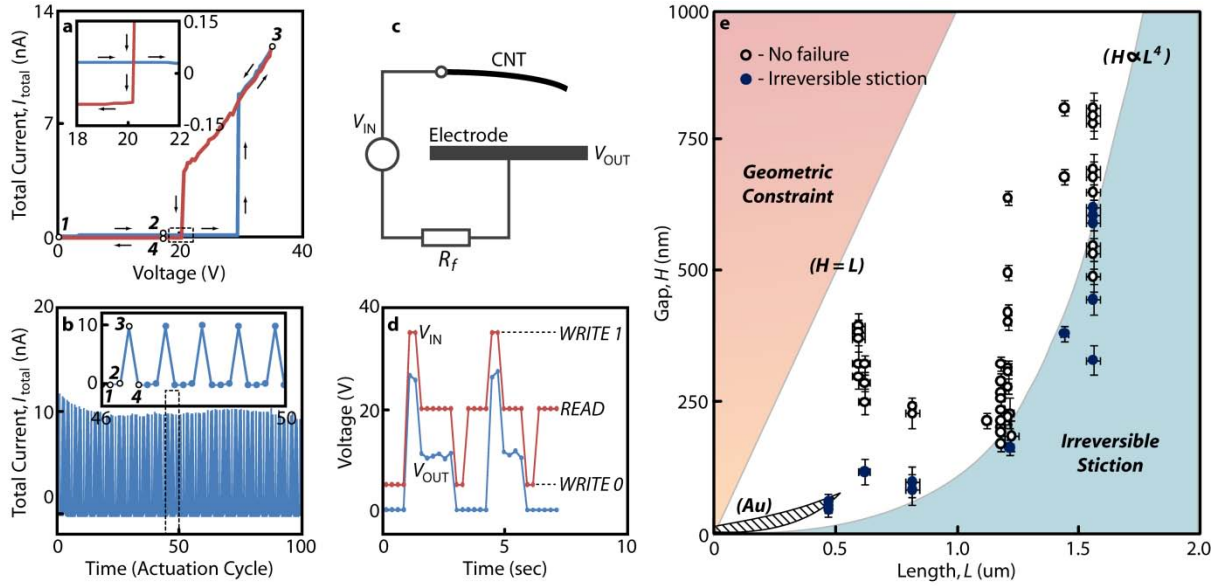


Figure 5 Suppressed failure modes and demonstrated device functionality using diamond-like carbon electrodes. (a) Characteristic I_{total} - V curve showing well-defined ON/OFF behavior with significantly less stiction than devices with gold electrodes. Inset shows detail of the pull-out event, after which the current is slightly negative due to gradual discharging of the capacitances, C_0 and C_{CNT} , as the applied voltage continues to decrease. (b) Current profile for 100 successive actuation cycles driven by a 0-35 V triangle wave at the voltage source. Inset shows a detail of cycles 46-50. The numbered data points correspond to the numbered positions in the I_{total} - V curve in (a). (c,d) Demonstration of basic volatile memory operation. (c) Schematic of voltage input (V_{IN}) used to write '0' or '1' and output (V_{OUT}). (d) Voltage input and measured output for a series of read and write operations. (e) Map of devices tested in the L - H geometric design space with ta-C electrodes. Incremental shortening/ablation is eliminated, while the onset of stiction is greatly suppressed as compared to those with gold electrodes. For comparison, the dashed area represents the robust, failure-free region determined for devices using gold electrodes (Figure 2f).

5. ELIMINATING FAILURE MODES THROUGH INFORMED DEVICE DESIGN

Given these positive predictions, devices with ta-C electrodes were then tested using the same *in situ* experimental technique (see Section 7.1). The characteristic I_{total} - V curves exhibited clean pull-in response and well-defined pull-out (Figure 5a) as compared to the gold electrodes (Figure 2a). The observation of sharper pull-out occurring earlier relative to the pull-in voltage suggests decreased CNT-electrode adhesion. This is reflected

in the map of failure modes (Figure 5c) where we see greatly suppressed onset of irreversible stiction along the L axis for a given H . This can be attributed to the relatively low surface energy and large contact angle of ta-C as compared to metals such as gold⁴⁰⁻⁴².

Perhaps more important though is the complete elimination of any observed incremental loss of CNT length during repeated actuation when using ta-C electrodes (Figure 5e). Even in devices in which the CNT-electrode gap approached the total length of the CNT, no shortening was observed. This elimination of observed shortening supports the model prediction of significant reduction of the current spike. Rather than being bound by charge dissipation, the design space is now limited by a less severe geometric constraint in which the CNT-electrode gap (H) simply cannot exceed the length (L) of the CNT.

To highlight the efficacy of this solution, a single device was tested through 100 successive actuation cycles by applying a triangle wave at the input voltage. Imaging the device before and after the 100 cycles showed no observable loss of length. Throughout the series of actuation cycles, the measured current versus time (Figure 5b) profile corresponds well to the current versus voltage measured before the cycles (Figure 5a). Given that the predicted mechanical stresses for the ta-C-based devices are similar to those of the Au-based devices, this successful high-cycle demonstration supports the model's hypothesis that mechanical stresses are not the cause of incremental CNT loss when Au electrodes are employed. It further supports the premise that charge dissipation-induced Joule heating is instead the key mechanism and demonstrates the efficacy of increasing CNT-electrode contact resistance in eliminating this failure mode.

To further demonstrate the functionality of the devices given their improved robustness, basic memory operation was tested. Treating the voltage source (Figure 1b and Figure 5c) as the input and the potential of the electrode as the output (Figure 5c) allows volatile storage of '0' and '1' states. Figure 5d shows a train of inputs and the corresponding measured output. To write '0', $V_{IN} < V_{PULL-OUT}$ causes the switch to open and V_{OUT} to go low. To write '1', $V_{IN} > V_{PULL-IN}$ causes the switch to close and V_{OUT} to go high. To read or store, $V_{PULL-OUT} < V_{IN} < V_{PULL-IN}$ holds the switch in its current state.

6. SCALING UP MANUFACTURING

To take full advantage of the robust CNT-based NEMS devices developed above, multiple devices operating in parallel are necessary. For example, simple OR logic requires two such two-state devices⁴³. Beyond individual logic operations, the ability to make numerous devices in parallel will allow for highly multiplexed sensors and other electronic devices. As with commonly-used electron beam lithography processes, the *in situ* nanomanipulation technique used herein to investigate failure modes of CNT-NEMS is not conducive to scaling up. Instead, scaling up requires the ability to create large, well-ordered arrays of individual CNTs in parallel.

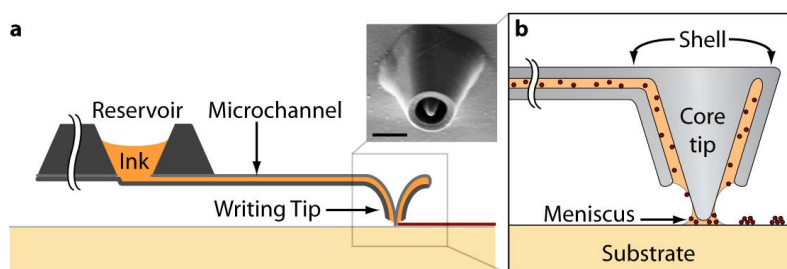


Figure 6 Schematic of nanoscale delivery using the Nano Fountain Probe⁴⁴. (a) Liquid ink is stored in an on-chip reservoir and fed through enclosed microchannels to apertured writing tips by capillary action. The inset shows a scanning electron microscopy (SEM) image of an apertured tip (scale bar is 2 μm). (b) For direct-write nanopatterning, the tip is brought into contact with the substrate where an ink meniscus forms.

To address this challenge within the objectives of this project, a unique probe-based nanomanufacturing tool called the Nano Fountain Probe (NFP⁴⁵⁻⁴⁶, Figure 6) was leveraged to create precise arrays of catalyst from which carbon nanotubes could subsequently be grown⁴⁷. The NFP, an atomic force microscopy (AFM) tool developed in the laboratory of the PI, functions like a highly miniaturized fountain pen to deliver liquid molecular “inks” with sub-100-nanometer resolution. These inks are loaded into an on-chip reservoir and fed through a series of enclosed microchannels to apertured writing tips (Figure 6). When the tip is brought into contact with the substrate, the ink forms a stable meniscus, allowing transport to the substrate for deposition (Figure 6b). By taking advantage of the precise spatial resolution of the AFM by which the NFP positioning is controlled during patterning, extremely precise arrays can be formed. Previously-demonstrated applications include nanopatterning of gold⁴⁸ and diamond⁴⁴ nanoparticles, biomolecules⁴⁹⁻⁵⁰, drugs⁴⁴, and thiol⁵¹ solutions on a variety of substrates.

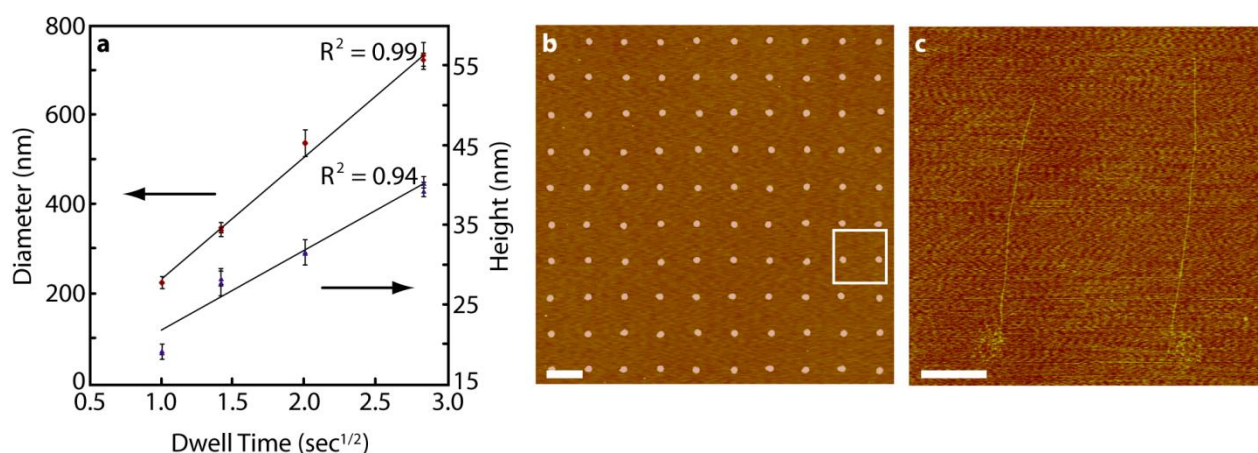


Figure 7 Nano Fountain Probe-based catalyst patterning for large-scale carbon nanotube arrays. (a) Feature size (dot diameter and height) as a function of square-root dwell time. (b) Dot array of catalyst patterned on a silicon dioxide substrate using the Nano Fountain Probe. Scale bar is 4 μm . (c) Two dots of catalyst from which carbon nanotubes have grown. Scale bar is 1 μm .

Arrays of catalyst were patterned on a variety of substrates using the NFP⁴⁷, including silicon, silicon dioxide, silicon nitride, quartz, and platinum. The ability to pattern precise dot arrays (Figure 7b) of three different catalyst types was demonstrated (iron(III) chloride, cobalt acetate, and ferritin). Feature size (dot diameter and height) showed strong dependence on the dwell time (Figure 7a), enabling precise control over the amount of catalyst deposited. Carbon nanotubes were then grown from the catalyst dots (Figure 7c) by chemical vapor deposition in a methane atmosphere at temperatures of 750 to 850 C.

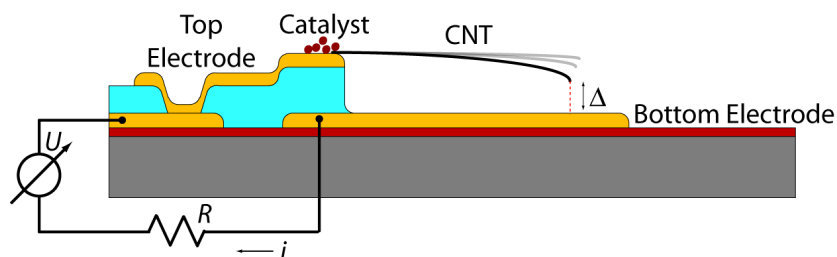


Figure 8 Schematic of a CNT-NEMS device fabricated using the Nano Fountain Probe-based catalyst patterning technique. First, all necessary electrodes, traces, vias, etc are constructed using conventional microfabrication techniques. As a final step, the Nano Fountain Probe is used to place the catalyst in desired locations and the carbon nanotubes grown in place.

This unique ability to create well-ordered arrays is now being integrated with a complete process flow to construct large numbers of the robust devices developed in Sections 3-5. Within this process, conventional microfabrication techniques are first used to create all necessary electrodes, traces, vias, etc. The NFP is then used to place catalyst in the locations where carbon nanotubes are desired (Figure 8). As a final step, the chips are placed in the CVD furnace and suspended nanotubes grown in place from the catalyst. This method of

device fabrication is unique in that it not only allows parallel fabrication of numerous devices, but also minimizes the exposure of the carbon nanotubes to harsh processing steps commonly used in microfabrication (e.g., strong etchants which can introduce defects in the nanotube structure) by placing the nanotube growth step at the end of the process flow. In contrast, most e-beam lithography processes to create freestanding nanotube structures make use of carbon nanotubes randomly dispersed on a sacrificial layer. After defining electrical contacts, the sacrificial layer is removed using strong chemical etchants (e.g., hydrofluoric acid) to release the nanotubes. When combined with the findings of the previous sections to eliminate prevalent failure modes (i.e., through the use of diamond-like carbon electrodes), these results will be a significant advance toward battle-ready NEMS.

7. SUMMARY AND SIGNIFICANT OUTCOMES

In summary, the limited reports of successful repeated actuation of CNT-based NEMS using conventional metal electrodes are not surprising given the prevalence of irreversible stiction and ablation failure modes throughout the design space as identified in this work. A dynamic multiphysics model of the device revealed that, in addition to the well-understood irreversible stiction, another dominant failure mode occurs due to Joule heating-induced ablation. This is the result of rapid dissipation of stored charges upon closing of the CNT switch. Together, these failure modes drastically confine the useful region of the geometric design space. We then showed that the robust, failure-free region of the design space is dramatically expanded through the use of alternative electrode materials such as diamond-like carbon. Using these diamond-like carbon electrodes, we see not only reduced stiction, but complete elimination of the ablation failure mode. This enables an unprecedented number of actuation cycles and reliable function as volatile memory, providing motivation for further implementation of alternative materials in improving performance, robustness, and reliability of electrostatically-actuated NEMS. Finally, given the efficacy of using diamond-like carbon electrodes in eliminating failure modes, we developed a probe-based nanomanufacturing scheme to create well-ordered arrays of individual carbon nanotubes. This will be integrated with a microfabrication process flow to construct large-scale arrays of robust CNT-based NEMS to enable parallel operation of these switches for logic operations.

To conclude, the significant outcomes from this project are:

1. Comprehensive identification of prevalent failure modes of CNT-based NEMS and their point of onset within the geometric design space using *in situ* electromechanical characterization.
2. Development of a dynamic multiphysics model which accurately captures the electromechanical response of the devices. This model, which was validated against experimental results, reveals the underlying mechanisms for the experimentally observed failure modes while enabling facile testing of potential solutions to these failure modes.
3. Dramatic improvement in device reliability by replacing commonly-used metal thin film electrodes with diamond-like carbon electrodes. This enabled hundreds of actuation cycles without failure and greatly expanded the usable region of the design space. This redesign of the device was based upon findings from the dynamic multiphysics model. A provisional patent application has been filed for this technology.
4. Development of a probe-based scheme for patterning arrays of catalyst for subsequent growth of carbon nanotubes in large, well-ordered arrays.

Ultimately, accomplishing these outcomes demonstrate the feasibility of transitioning CNT-NEMS from the lab bench to the battle field in the form of *truly robust, highly functional* devices.

8. METHODS

8.1 *In Situ Device Characterization*

In situ electromechanical device characterization was conducted in a Nova NanoSEM (FEI) scanning electron microscope (SEM) for simultaneous high resolution imaging and current-voltage measurements. Arc-discharge-grown multi-walled CNTs (n-Tec, Norway) were first dispersed in dry powder form on a copper TEM grid (Structure Probe, Inc). The grid was mounted on a Teflon block and placed in the SEM. SEM imaging was used to identify protruding CNTs of the desired length and diameter for device characterization (for all experiments, CNTs of consistent radius (21 ± 3 nm) were selected to allow direct comparison of results between devices of varying length and gap). A 3-axis piezoelectric nanomanipulator (Klocke Nanotechnik, Germany) mounted inside the SEM was then used to bring a sharpened tungsten probe (Micromanipulator Co., USA) into contact with the free end of the selected CNT. Electron beam-induced deposition of carbon was used to fix the CNT in place on the tip of the probe. This deposition technique has been shown to produce near-ideal Ohmic contacts to CNTs⁵². The nanomanipulator was then used to extract the cantilevered CNT and bring it into close proximity to the electrode (also mounted on the same Teflon block to electrically isolate it from the SEM stage). This effectively recreated the platform device geometry (Figure 1a) with the CNT-electrode gap being precisely controlled by the position of the nanomanipulator probe relative to the electrode (Figure 1c).

The probe and electrode were electrically addressable via a feedthrough in the SEM chamber wall. The circuit was completed by insertion of a 1 G Ω resistor (Ohmite Mini-Mox, 992 M Ω actual measured resistance) in line between the electrode and SEM chamber feedthrough. An electrical bias was applied and current simultaneously measured using a parameter analyzer (Keithley 4200-SCS Semiconductor Characterization System). During $I_{\text{total}}-V$ measurements, the electron beam of the SEM was blanked as it typically generated noise in the measurements as high as 0.5 nA.

The CNTs were imaged before and after actuation to inspect for failure. CNT length and diameter, and CNT-electrode gap were measured from SEM images using ImageJ software (NIH). The CNT diameter was taken from the full width at half max of the intensity profile across the cross section of the CNT in the image.

8.2 Electrode Fabrication

Gold electrodes were fabricated by depositing a 100-nm film of gold (with a 10 nm chromium adhesion layer) on a 200-nm-thick silicon nitride-coated silicon wafer by thermal evaporation. A 1-cm² piece was then cleaved from the wafer and fixed to the Teflon block as described above. Ta-C electrodes were fabricated by depositing a 140-nm film of ta-C on similar silicon nitride-coated silicon wafer. To define the proper total electrode resistance and eliminate the need for the external 1 G Ω resistor, long thin traces of ta-C were patterned in the ta-C film. First, a 70-nm aluminum film (with a 10-nm titanium adhesion layer) was deposited by evaporation over the ta-C and patterned by photolithography and liftoff. This was used as an etch mask to define the ta-C electrode shape. The exposed ta-C was etched through to the silicon nitride by reactive ion etching (RIE) using CF₄/O₂. The aluminum etch mask was then stripped by RIE using BCl₃/Cl₂/He to re-expose the ta-C electrodes. Finally the ta-C sample was mounted on a Teflon block in place of the gold electrode.

8.3 Measuring Parameters for Multiphysics Model

The multiphysics models require knowledge of the parasitic capacitance and CNT-electrode contact resistances. These were measured experimentally to improve the quantitative accuracy of the models. To measure the parasitic capacitance, the nanomanipulator was first used to bring a CNT into close proximity with the electrode as before. The Keithley 4200-SCS system was then used to source a constant current of 30 fA while measuring the corresponding rise in voltage required to source this current. Assuming the parasitic capacitance is significantly larger than the CNT-electrode capacitance ($C_0 \gg C_{CNT}$, where C_{CNT} is on the order of 10⁻¹⁷ F¹²) the parasitic capacitance was estimated based upon the time required to ramp from 0 to 1 V at constant current ($C_0 \approx i \cdot \Delta t / \Delta V$). This yielded a parasitic capacitance of about 50 pF for both the Au- and ta-C-electrode systems.

The measured parasitic capacitance was validated by comparison to the capacitance predicted based upon the magnitude of the slightly negative current observed after pull-out (insets of Figure 2d and Figure 5a). After pull-out, the switch is open again at which point the only current expected would be due to discharging of the parasitic capacitance in response to the continued decrease in applied voltage. Given a fixed value of

capacitance, this current is proportional to the rate which the voltage was ramped down ($i \approx C_0 \cdot \Delta V / \Delta t$). In these experiments, the voltage was ramped down at a rate of -2.2 V/s which, given a capacitance of 50 pF, would yield a current of -0.11 nA as the voltage is ramped down. This compares favorably to the experimentally measured currents of approximately -0.1 nA after pull-out, adding confidence to the values used for parasitic capacitance.

The contact resistance was estimated first by taking the slope of the I_{total} - V curve after pull-in to calculate the total circuit resistance. From this, the total circuit resistance when the tungsten probe was pressed into direct contact with the electrode (no CNT present) was subtracted to yield the CNT-electrode contact resistance. This calculation is based upon the assumption that the probe-electrode contact resistance is significantly less (because the area of contact is orders of magnitude greater) than the CNT-electrode contact resistance. This yielded a CNT-electrode contact resistance of $R_c = 5$ -50 k Ω for gold, and $R_c = 0.6$ G Ω for ta-C. Note that in the equivalent lumped element circuit (Figure 1b), the combined tunneling/contact resistance term ($R_{CNT} = R_c \exp(\lambda\delta)$, where δ is the gap between the CNT and substrate) approaches R_c as $\delta \rightarrow 0$ (see Section 4.1).

9. REFERENCES

- 1 International Roadmap Committee. The international technology roadmap for semiconductors. (2009).
- 2 Rueckes, T., Kim, K., Joslevich, E., Tseng, G. Y., Cheung, C. & Lieber, C. M. Carbon nanotube-based nonvolatile random access memory for molecular computing. *Science* **289**, 94-97 (2000).
- 3 Cha, S., Jang, J., Choi, Y., Amaratunga, G., Kang, D. J., Hasko, D., Jung, J. & Kim, J. Fabrication of a nanoelectromechanical switch using a suspended carbon nanotube. *Applied Physics Letters* **86** (2005).
- 4 Collins, P., Arnold, M. & Avouris, P. Engineering carbon nanotubes and nanotube circuits using electrical breakdown. *Science* **292**, 706-709 (2001).
- 5 Murali, R., Yang, Y., Brenner, K., Beck, T. & Meindl, J. Breakdown current density of graphene nanoribbons. *Applied Physics Letters* **94**, 243114 (2009).
- 6 Hayamizu, Y., Yamada, T., Mizuno, K., Davis, R., Futaba, D., Yumura, M. & Hata, K. Integrated three-dimensional microelectromechanical devices from processable carbon nanotube wafers. *Nature Nanotechnology* **3**, 289-294 (2008).
- 7 Smith, R., Rueckes, T., Konsek, S., Ward, J., Brock, D. & Segal, B. Carbon nanotube based memory development and testing. *in IEEE Aerospace* 1-5 (2007).
- 8 Ke, C. H. & Espinosa, H. D. In-situ Electron Microscopy Electro-Mechanical Characterization of a NEMS Bistable Device. *Small* **2**, 1484-1489 (2006).
- 9 Ke, C. H. & Espinosa, H. D. Feedback controlled nanocantilever device. *Applied Physics Letters* **85**, 681-683 (2004).
- 10 Ke, C. H., Pugno, N., Peng, B. & Espinosa, H. D. Experiments and modeling of carbon nanotube-based NEMS devices. *Journal of the Mechanics and Physics of Solids* **53**, 1314-1333 (2005).
- 11 Ke, C. H. & Espinosa, H. D. Numerical analysis of nanotube based NEMS devices - Part I: Electrostatic charge distribution on multiwalled nanotubes. *Journal of Applied Mechanics* **72**, 721-725 (2005).

- 12 Ke, C. H., Espinosa, H. D. & Pugno, N. Numerical analysis of nanotube based NEMS devices - Part II: Role of finite kinematics, stretching and charge concentrations. *Journal of Applied Mechanics* **72**, 726-731 (2005).
- 13 Ke, C. *Development of a feedback controlled carbon nanotube based nanoelectromechanical device* PhD thesis, Northwestern University, (2006).
- 14 Ke, C. H. & Espinosa, H. D. in *Handbook of Theoretical and Computational Nanotechnology* (2005).
- 15 Espinosa, H. D., Ke, C. & Pugno, N. in *Encyclopedia of Materials: Science and Technology* (ed Patrick Veyssiere) (Elsevier, 2006).
- 16 Lee, S., Lee, D., Morjan, R., Jhang, S., Sveningsson, M., Nerushev, O., Park, Y. & Campbell, E. A three-terminal carbon nanorelay. *Nano Letters* **4**, 2027-2030 (2004).
- 17 Li, Q., Koo, S.-M., Edelstein, M., Suehle, J. & Richter, C. Silicon nanowire electromechanical switches for logic device application. *Nanotechnology* **18**, 315202 (2007).
- 18 Li, M., Bhiladvala, R., Morrow, T., Sioss, J., Lew, K.-K., Redwing, J., Keating, C. & Mayer, T. Bottom-up assembly of large-area nanowire resonator arrays. *Nature Nanotechnology* **3**, 88-92 (2008).
- 19 Marcus, M., Simmons, J., Baker, S., Hamers, R. & Eriksson, M. Predicting the Results of Chemical Vapor Deposition Growth of Suspended Carbon Nanotubes. *Nano Letters* **9**, 1806-1811 (2009).
- 20 Deshpande, V., Chiu, H.-Y., Postma, H. W. C., Miko, C., Forro, L. & Bockrath, M. Carbon nanotube linear bearing nanoswitches. *Nano Letters* **6**, 1092-1095 (2006).
- 21 Hertel, T., Walkup, R. & Avouris, P. Deformation of carbon nanotubes by surface van der Waals forces. *Physical Review B* **58**, 13870-13873 (1998).
- 22 Martel, R., Schmidt, T., Shea, H., Hertel, T. & Avouris, P. Single- and multi-wall carbon nanotube field-effect transistors. *Appl. Phys. Letts.* **73**, 2447-2449 (1998).
- 23 Wei, W., Liu, Y., Wei, Y., Jiang, K., Peng, L.-M. & Fan, S. Tip cooling effect and failure mechanism of field-emitting carbon nanotubes. *Nano Letters* **7**, 64-68 (2007).
- 24 Wang, Z., Gao, R., de Heer, W. & Poncharal, P. In situ imaging of field emission from individual carbon nanotubes and their structural damage. *Appl. Phys. Letts.* **80**, 856-858 (2002).
- 25 Doytscheva, M., Kaiser, M. & de Jonge, N. In situ transmission electron microscopy investigation of the structural changes in carbon nanotubes during electron emission at high currents. *Nanotechnology* **17**, 3226-3233 (2006).
- 26 Jang, W., Lee, J., Yoon, J.-B., Kim, M.-S., Lee, J.-M., Kim, S.-M., Cho, K.-H., Kim, D.-W., Park, D. & Lee, W.-S. Fabrication and characterization of a nanoelectromechanical switch with 15-nm-thick suspension air gap. *Appl. Phys. Letts.* **92**, 103110 (2008).
- 27 Dequesnes, M., Tang, Z. & Aluru, N. Static and dynamic analysis of carbon nanotube-based switches. *Journal of Engineering Materials and Technology* **126**, 230 (2004).
- 28 Jonsson, L., Axelsson, S., Nord, T., Viefers, S. & Kinaret, J. High frequency properties of a CNT-based nanorelay. *Nanotechnology* **15**, 1497-1502 (2004).
- 29 Poncharal, P., Wang, Z. L., Ugarte, D. & de Heer, W. A. Electrostatic deflections and electromechanical resonances of carbon nanotubes. *Science* **283**, 1513-1516 (1999).
- 30 Wu, Y.-C. & Adams, G. A robust analysis of the actuation of a carbon-nanotube-based nanoswitch with sidewall slip. *J. Appl. Phys.* **106**, 054310 (2009).
- 31 Lennard-Jones, J. Perturbation problems in quantum mechanics. *Proceedings of the Royal Society of London. Series A, Containing Papers of a Mathematical and Physical Character*, 598-615 (1930).
- 32 Girifalco, L., Hodak, M. & Lee, R. Carbon nanotubes, buckyballs, ropes, and a universal graphitic potential. *Physical Review B* **62**, 13104-13110 (2000).
- 33 Erbe, A., Blick, R., Tilke, A., Kriele, A. & Kotthaus, J. A mechanically flexible tunneling contact operating at radio frequencies. *Applied Physics Letters* **73**, 3751 (1998).
- 34 Peng, B., Locascio, M., Zapol, P., Li, S., Mielke, S. L., Schatz, G. C. & Espinosa, H. D. Measurements of near-ultimate strength for multiwalled carbon nanotubes and irradiation-induced crosslinking improvements. *Nature Nanotechnology* **3**, 626 - 631, doi:doi:10.1038/nnano.2008.211 (2008).

- 35 Blakslee, O., Proctor, D., Seldin, E., Spence, G. & Weng, T. Elastic Constants of Compression Annealed Pyrolytic Graphite. *Journal of Applied Physics* **41**, 3373 (1970).
- 36 Javey, A., Qi, P., Wang, Q. & Dai, H. Ten-to 50-nm-long quasi-ballistic carbon nanotube devices obtained without complex lithography. *Proceedings of the National Academy of Sciences of the United States of America* **101**, 13408 (2004).
- 37 Kinaret, J., Nord, T. & Viefers, S. A carbon-nanotube-based nanorelay. *Applied Physics Letters* **82**, 1287-1289 (2003).
- 38 Jang, J., Cha, S., Choi, Y., Amaratunga, G., Kang, D., Hasko, D., Jung, J. & Kim, J. Nanoelectromechanical switches with vertically aligned carbon nanotubes. *Appl. Phys. Lett.* **87** (2005).
- 39 Jang, J., Cha, S., Choi, Y., Kang, D., Butler, T., Hasko, D., Jung, J., Kim, J. & Amaratunga, G. Nanoscale memory cell based on a nanoelectromechanical switched capacitor. *Nature Nanotechnology* **3**, 26-30 (2008).
- 40 Luo, J., Fu, Y., Le, H., Williams, J., Spearing, S. & Milne, W. Diamond and diamond-like carbon MEMS. *Journal of Micromechanics and Microengineering* **17**, S147-S163 (2007).
- 41 Kwok, S., Wang, J. & Chu, P. Surface energy, wettability, and blood compatibility phosphorus doped diamond-like carbon films. *Diamond and Related Materials* **14**, 78-85 (2004).
- 42 Needs, R. & Mansfield, M. Calculations of the surface stress tensor and surface energy of the (111) surfaces of iridium, platinum and gold. *J. Phys.: Condens. Matter* **1**, 7555-7563 (1989).
- 43 Huang, Y., Duan, X. F., Cui, Y., Lauhon, L. J., Kim, K. H. & Lieber, C. M. Logic gates and computation from assembled nanowire building blocks. *Science* **294**, 1313-1317 (2001).
- 44 Loh, O., Lam, R., Chen, M., Moldovan, N., Huang, H., Ho, D. & Espinosa, H. Nanofountain Probe-Based High Resolution Patterning and Single Cell Injection of Functionalized Nanodiamonds. *Small* **5**, 1667-1674 (2009).
- 45 Moldovan, N., Kim, K. H. & Espinosa, H. D. Design and fabrication of a novel microfluidic nanoprobe. *J. MEMS* **15**, 204-213 (2006).
- 46 Moldovan, N., Kim, K.-H. & Espinosa, H. D. A multi-ink linear array of nanofountain probes. *J. Micromech. Microeng.* **16**, 1935-1942 (2006).
- 47 Loh, O., Safi, A. & Espinosa, H. Direct-write catalyst patterning for large-scale carbon nanotube device arrays. (in preparation).
- 48 Wu, B., Ho, A., Moldovan, N. & Espinosa, H. D. Direct deposition and assembly of gold colloidal particles using a nanofountain probe. *Langmuir* **23**, 9120-9123 (2007).
- 49 Kim, K.-H., Sanedrin, R. G., Ho, A. M., Lee, S. W., Moldovan, N., Mirkin, C. A. & Espinosa, H. D. Direct Delivery and Submicrometer Patterning of DNA by a Nanofountain Probe. *Adv. Mater.* **20**, 330-334 (2008).
- 50 Loh, O., Ho, A., Rim, J., Kohli, P., Patankar, N. & Espinosa, H. Electric field-induced direct delivery of proteins by a nanofountain probe. *PNAS* **105**, 16438-16443 (2008).
- 51 Kim, K. H., Moldovan, N. & Espinosa, H. D. A nanofountain probe with sub-100 nm molecular writing resolution. *Small* **1**, 632-635 (2005).
- 52 Wang, Y., Wang, T., Lin, X. & Dravid, V. Ohmic contact junction of carbon nanotubes fabricated by in situ electron beam deposition. *Nanotechnology* **17**, 6011-6015 (2006).